Applied Materials Today 44 (2025) 102762

Contents lists available at ScienceDirect

Applied Materials Today

journal homepage: www.elsevier.com/locate/apmt

Detection of magnetic field polarity with magnetic field modulation ODMR on NV⁻ centers in diamond

Fabrizio Moro

Department of Materials Science, University of Milano-Bicocca, Milano, 20125, Italy

ARTICLE INFO

Keywords:
Magnetic field polarity
NV- centers in diamond
Magnetic resonance
Colour centers
Magnetometry

ABSTRACT

Diamond with negatively charged nitrogen-vacancy (NV^-) colour centers is a promising material system for quantum sensing applications and in particular for magnetometry. The sensing protocol leverages on optically detected magnetic resonance (ODMR) technique which provides high sensitivity to magnetic field magnitude and orientation from the analysis of the resonance frequencies. Direct detection of the magnetic field polarity would be appealing for the study of physical phenomena and applications where real-time detection of static and dynamic stray field from samples is required. Unfortunately, ODMR resonance lines are inherently insensitive to the magnetic field polarity. Here, an effect has been observed where the ODMR spectra recorded for an ensemble of NV^- centers by demodulating a small magnetic field (B_{mod}-ODMR) directly correlates the symmetry of the first-derivative spectral lines to the magnetic field polarity. A model is introduced to explain the mechanism underlying for B_{mod}-ODMR along with a *proof-of-concept* for real-time detection of magnetic field switching.

1. Introduction

Quantum sensors are devices that leverage the principles of quantum mechanics to measure physical quantities with unprecedented precision and sensitivity with respect to their classical counterparts. There is a variety of quantum sensors based on superconductors, cold atoms, topological insulators to name a few, each with its own pros and cons in terms of sensitivity and spatial resolution. Negatively charged nitrogen-vacancy (NV^-) color centers in diamond crystals [1] stand out because of their unique properties such as chemical, electrical and optical stabilities [2] as well as long spin coherence times at room temperature [3]. These exceptional properties make NV^- centers suitable for precise measurements of magnetic fields [4], electric fields, [5] temperature [6], and pressure [7]. Thus, NV^- centers in diamond represent a platform for applications across various fields including quantum information [3, 8], biological imaging [9], nano MRI [10], navigation[11], materials science[12] as well as for the exploration of novel phenomena in physics such as topological currents [13] and magnetic skyrmions [14].

Particularly promising is their use in quantum magnetometry [15, 16] with magnetic field sensitivity down to pico-tesla [1], as well as quantum imaging [15] with spatial resolution scalable down to nanometers. Magnetic field measurements are possible because the separation between the magnetic resonance frequencies of the NV^- spin ground state ($S = 1$) increases with the intensity of the magnetic field. Furthermore, the four inequivalent quantization axes of the NV^- centers due to the diamond tetrahedral symmetry enable the reconstruction of the magnetic field directions [17]. The technique employed is called optically detected magnetic resonance (ODMR) and relies on the detection of changes of the fluorescence upon magnetic resonance condition [18–20]. From the fitting of resonance peaks, the magnetic field vector magnitude and directions can be reconstructed [17]. ODMR is a well-known and powerful technique traditionally employed to study optically active defects and spin dependent recombination processes in semiconductors [18] such as SiC [21,22], hBN [23], GaN [19], quantum dots [24–26] organic molecules [27] for quantum computing, quantum sensing, singe photon emitters as well as MASER applications.

Unfortunately, the sign of the ODMR spectral lines is inherently independent on the magnetic field directions. Furthermore, the complex spectral analysis of the ODMR spectra hinders direct access to the magnetic field polarity as well as real-time detection. This limitation can be suppressed either by using circularly polarized microwave excitation (σ^+ or σ^-) in order to address a given electron spin transition [28], or by applying a constant bias magnetic field [16,29].

Here, a method is reported where ODMR spectra are recorded by demodulating an oscillating small magnetic field in combination with linearly polarized microwaves. The results show that the locking of the modulation phase to the spin-dependent photoluminescence enables direct detection of magnetic field polarities simply by reading-off the

E-mail address: fabrizio.moro@unimib.it.

https://doi.org/10.1016/j.apmt.2025.102762
Received 9 January 2025; Received in revised form 6 April 2025; Accepted 1 May 2025
Available online 8 May 2025

sign of the ODMR spectral lines.

In the following, ODMR studies in a microdiamond with NV^- centers are presented, and a model is introduced to explain the phenomenology. Finally, a *proof-of-concept* for real-time detection of slowly switching magnetic field polarities is provided.

2. Results and discussion

Fig. 1a shows the molecular structure of a NV^- center with its C_{3v} symmetry with respect to the laboratory frame x_L, y_L, z_L. The nitrogen atom can replace any of the 4 carbon sites in the tetrahedron, thus providing four inequivalent NV^- centers (*i.e.* NV1, NV2, NV3 and NV4) each with its own spin quantization axis. In Fig. 1b is reported the Jablonski diagram with the $S = 1$ ground ($^3A_2$) and excited (^3E) states which are zero-field split by axial (D) and rhombic (E) distortions. In zero magnetic field the four NV^- site are magnetically equivalent. When an external magnetic field is applied the energy levels are split by Zeeman interaction and each NV^- site experiences a different magnetic field projection, thus resulting in 4 doublets. The nuclear spin of ^{14}N contributes to a further splitting of the energy levels for each doublet.

Optical pumping with green light (532 nm) of $^3A_2$ to vibronic levels of ^3E leads to spin conversing radiative decay back to the ground state emitting photons in the red region of the electromagnetic spectrum. The $^3E(m_s = \pm1)$ states mostly decay to the $^3A_2(m_s = \pm1)$ states but a significant portion decays non-radiatively to the singlet ^1A state. These non-radiative transitions occur more rapidly from the $^3E(m_s = \pm1)$ states than from $^3E(m_s = \pm 0)$. Singlet-singlet transition $^1A_1 \rightarrow {}^1E$ takes place with almost all the energy being transferred non-radiatively and a small portion of the transitions occur via emission of infrared radiation. Finally, non-radiative $^1E \rightarrow {}^3A_2$ transitions occur with roughly equal transition probabilities. As result of the differences between the radiative and non-radiative transition rates of the $^3E(m_s = 0)$ and $^3E(m_s = \pm1)$ states, after several excitation-relaxation cycles the population of $^3A_2$ results strongly polarized in the $m_s = 0$ sublevel. Under this condition, the resonant excitation of the m_s states with powerful microwaves radiation saturates the $m_s = \pm1$ states leading to a depolarization of the $^3A_2(m_s = 0)$ level, with a consequent quenching of the photoluminescence (PL). Saturation of the $m_s = \pm1$ states is in practice rarely achieved because of inhomogeneously broadened lines [18]. Thereby, magnetic resonance transitions can be detected by monitoring the PL signal as function of the microwave frequency, thus providing the ODMR spectrum.

The scheme of the ODMR technique is shown in Fig. 1c, and further details of the set-up are given in the section METHODS. In brief, a green laser beam is reflected by a dichroic mirror and focused on a diamond microcrystal mounted on a microstripline. Photoluminescence is detected through the objective, the dichroic mirror and it is focused on a photodiode. The current signal is amplified and fed into a lock-in amplifier and an oscilloscope interfaced with a PC for data acquisition.

Fig. 2a reports the high resolution experimental spectra recorded with and without magnetic field modulation for an arbitrary angle in a small DC magnetic field ($\vec{B}$). The former is hereafter referred to B_{mod}-ODMR (Fig. 1d). Both spectra show four resonance pairs symmetrically distributed around the frequency $D = 2870$ MHz, and ascribed to the four inequivalent NV^- crystallographic sites. The difference in the resonance frequencies is due to the magnetic field projection, $\vec{B}_{NV}$, experienced by each NV^- site along the quantization axis which is larger for the outer pairs and smaller for the inner pairs. The resonant lines are in-homogeneously broadened as well as broadened by ^{14}N hyperfine interactions as it can be clearly seen in the three resolved evenly spaced resonances for NV3 in the B_{mod}-ODMR spectrum. These features correspond to electron-nuclear spin transitions shown in Fig. 1b. The ODMR spectrum recorded without modulation field (bottom spectrum of Fig. 2a) shows quenching of PL, *i.e.* negative ODMR contrast, for all the NV^- sites with a contrast decreasing from NV1 to NV4. The B_{mod}-ODMR spectrum shows first derivative-like signals due to the mixing of the modulated PL signal by the oscillating magnetic field. However, the resonance lines have opposite symmetries indicated with symbols + and – corresponding to positive/negative and negative/positive signs respectively with ascending sweep of the microwave frequencies. The signal intensities decrease from NV1 to NV4 as also observed for the unmodulated ODMR spectrum.

For small magnetic fields, the $m_s = 0$ state is the ground state, whereas at magnetic fields higher than 50 mT anti-crossing between the $m_s = 0$ and the $m_s = -1$ levels occurs [30,31]. This is supported by spin dynamics studies in zero magnetic field which have shown a preferential population of the $m_s = 0$ state [32]. Thus, the negative ODMR contrast is a fingerprint for microwave absorption due to the transition of the electrons from the $m_s = 0$ state to the $m_s = -1$ and $+1$ states. This is also expected from the ODMR mechanisms where many cycles of optical pumping tend to fully polarize the $m_s = 0$ state. Conversely, an increase of PL (*i.e.* positive ODMR contrast) would have corresponded to preferential photon emission, hence to opposite transitions. On the other hand, the opposite symmetries of the resonance lines in the B_{mod}-ODMR spectrum are fingerprint for absorptive (+) and emissive (–) microwave

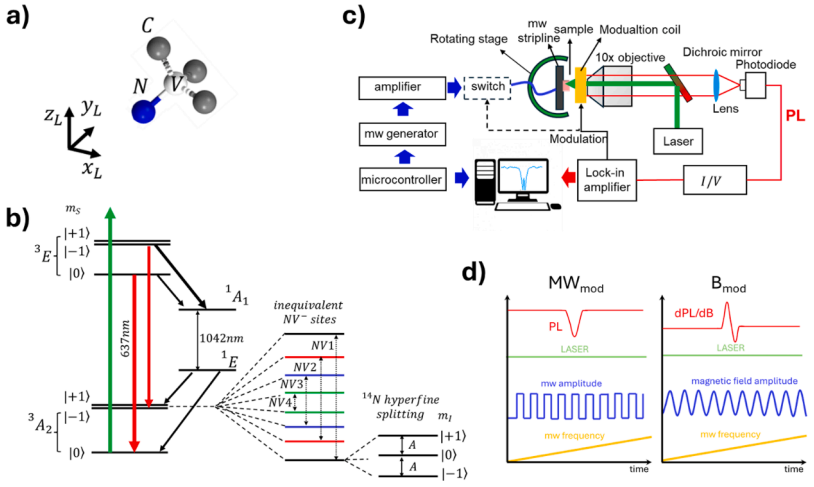

Fig. 1. a) Structure of a NV^- center in the diamond crystal and laboratory frames. **b)** Energy level diagram of a NV^- center ($S = 1$) with axial and rhombic zero field splitting $D = 2870$ MHz and $E = 7$ MHz respectively and ^{14}N hyperfine interaction A. Arrows thickness stands for different transitions probabilities. Splitting of the $m_s = \pm1$ sublevels due to inequivalent NV^- sites is also shown. **c)** Scheme of the ODMR set-up spectra with magnetic field modulation (B_{mod}) and microwave amplitude modulation (MW_{mod}, see components with dashed lines.) **d)** Detection scheme for ODMR with MW_{mod} and B_{mod} (see METHODS).

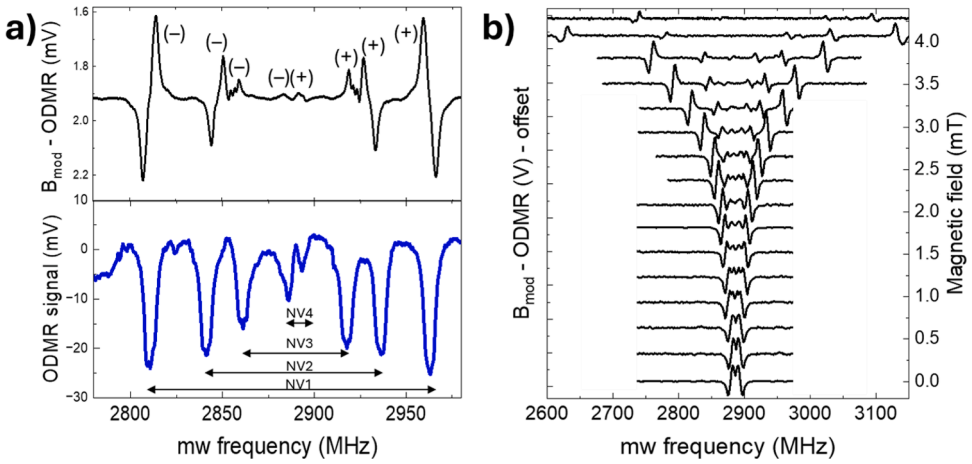

Fig. 2. **a)** Experimental ODMR spectra recorded with (black curve) and without magnetic field modulation (blue curve) for an arbitrary angle, $\varphi = 80°$ in the xz plane of the laboratory frame with external magnetic field $|\vec{B}| \sim 3.2$ mT (step = 0.5 MHz). The positive and negative ODMR contrasts and resonance pairs for magnetically inequivalent NV^- centers are indicated. **b)** Magnetic field dependent spectra for $|\vec{B}|$ varying from 0 mT (bottom spectrum) to 4 mT (top spectrum).

transitions in out-of-equilibrium population of the energy levels often observed in organic triplets [33,34]. It has been found that optical pumping in NV^-centers induces out-of-equilibrium population of the m_s states leading to absorptive (+) and emissive (–) resonance lines strongly dependent on the relative orientation of the magnetic field and the NV^- quantization axis [33,35–37]. Thus, the negative contrast of all the transitions in the ODMR spectrum and for all the NV^- sites is in apparent contradiction with the opposite symmetries observed for the resonances in the B_{mod}-ODMR spectrum.

In order to achieve a deeper understanding, phase sensitive lock-in detection was performed with modulation of the microwave (MW_{mod}) and magnetic field amplitudes (B_{mod}) under the same conditions (Fig. 1d). First of all, the spectra were recorded as function of the applied magnetic field intensity (Fig. 2b). The B_{mod}-ODMR spectrum at zero field reveals only two first derivative signals as result of the fine rhombic splitting ($E \sim 7$ MHz) of the $m_s = \pm 1$ states occurring from magnetically equivalent NV^- centers in absence of magnetic field. Furthermore, the symmetry of these two signals is opposite.

It is worth noting that at zero field the lock-in signal results from the modulation of background magnetic field (*i.e.* earth magnetic field). By increasing the magnetic field the two peaks depart in opposite frequency directions all the way up to 4 mT, and split in four doublets due to the different projections of the magnetic field on the 4 possible coordination of the NV^- centers in the diamond crystal structure. The sign of each resonance peak is consistently linked to the spin resonance transition, either $m_s = 0 \rightarrow +1$ or $0 \rightarrow -1$, across the whole spanned microwave frequency and magnetic field ranges. Thus, for a fixed direction of the magnetic field, the $m_s = 0 \rightarrow +1$ and $m_s = 0 \rightarrow -1$ transitions can be unambiguously discerned by their resonance frequencies as well as by the symmetry of the corresponding ODMR signals recorded with magnetic field modulation.

Angular dependent studies were performed both in B_{mod} (Fig. 3a) and MW_{mod} (see **Figure S1**) and by rotating a permanent magnet in the x_Lz_L laboratory plane (that is around the y_L axis) and recording ODMR

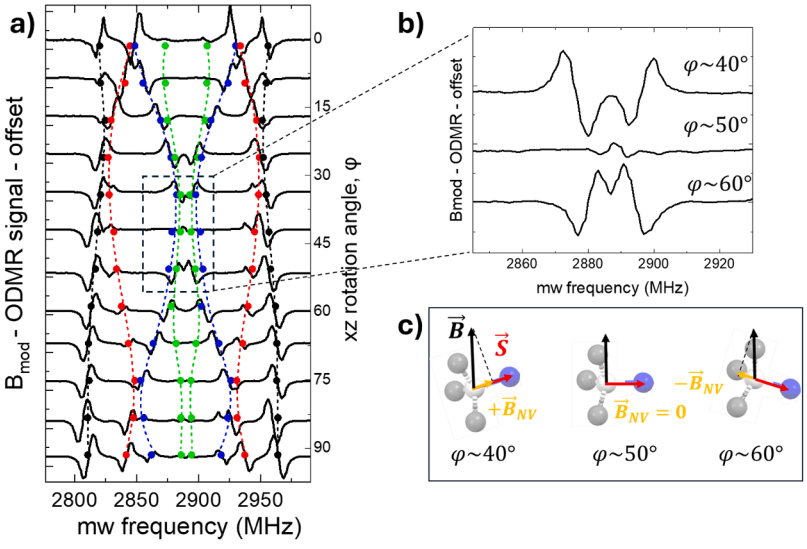

Fig. 3. **a)** B_{mod}-ODMR by rotating a permanent magnet ($|\vec{B}| \sim 3$ mT) in the xz laboratory plane. The dots are the extracted microwave resonance frequencies from the simulations of the ODMR spectra in **Figure S1** and the continuous lines are the interpolations. Color code: NV1 = black dots, NV2 = red dots, NV3 = blue dots, NV4 = green dots. **b)** Zoom of the ODMR spectral lines around the frequency range $\sim D$ and for $40° < \varphi < 60°$. **c)** Visualization of the applied field $\vec{B}$ and its projection $\vec{B}_{NV}$ on the NV^- spin quantization axis S for the angles $\varphi = 40°$, 50° and 60° The switching of the magnetic field projections $\vec{B}_{NV}$ on a NV^- center from parallel to antiparallel to S is observed.

spectra for different angles φ at fixed magnetic field $|\vec{B}| \sim 3$ mT. With this experiment, it is investigated the correlation between the first derivative sign + or – and the 0 → +1 or 0 → –1 spin transitions in the magnetic switching regime, that is where $\vec{B}_{NV}$ for each of the four inequivalent NV^- centers turn from parallel to antiparallel direction with respect to $\vec{S}$.

The results reported in Fig. 3a show that the resonance frequencies of the four doublets moves smoothly with φ in a not trivial manner. The random orientation of the microcrystal hinders a simple understanding of the particular pattern followed by the 4 doublets especially for the B_{mod}-ODMR spectra where the intensities of some peaks appear to decrease within a certain angle range (*e.g.* anti-crossing points). The MW_{mod}-ODMR spectra show consistently negative contrast and cancellation of resonances with opposite symmetry is avoided, thus making possible to track all the resonances across the entire frequency spectrum and rotation angles. Therefore, the MW_{mod}-ODMR spectra were first simulated to extract the resonance frequencies for each spectrum and then overlayed to the corresponding B_{mod}-ODMR spectra for comparison. The only fit-parameters were the Euler angles (α, β, γ) of the crystal frame relative to the laboratory frame by keeping the molecular frame fixed to (45° 54° 0) with respect to the crystal frame (**Table S1** and METHODS). The road map in Fig. 3a shows that the resonance frequencies corresponding to the sites NV1 and NV4 experience a weaker angular dependence compared to the resonance frequencies for the sites NV2 and NV3, thus suggesting that the magnetic field is mostly spinning around their quantization axis. For $\varphi \sim 30^\circ$ the NV1 / NV2 and NV3 / NV4 resonances overlap and only four peaks can be distinguished. For $\varphi \sim 50^\circ$ the inner resonances NV3 and NV4 shift towards the center of gravity of the spectrum and after a critical angle the resonance lines re-emerge with an apparent inverted symmetries, that is from + to – when φ changes from 40° to 60°. A closer look at the spectra in the range $\varphi \sim 40^\circ - 60^\circ$ (Fig. 3b) reveals that the NV3 and NV4 resonances overlap and their intensities cancel out because of their opposite symmetries.

From a geometrical/structural viewpoint the symmetry inversion at the turning point for NV3 and NV4 can be explained by considering the magnetic field projection $\vec{B}_{NV}$ on the NV^- quantization axis, $\vec{S}$ (Fig. 3c). The Euler angles obtained from the simulations provide a complete picture of the fields and their correlations with the ODMR spectral lines. When $\vec{B}$ is oriented off to one of the spin axis, the m_s states are no longer *good* quantum numbers and the eigenstates of the spin Hamiltonian are mixed [38]. As a result, the B_{mod}-ODMR contrast vanishes as it can be observed by the gradual decrease of the ODMR signal from the NV1 to the NV4 resonances (Fig. 2a).

When $\vec{B}_{NV}$ becomes anti-parallel to $\vec{S}$, the m_s states are swapped for inversion of the magnetic field, and this is accompanied by the inversion symmetry of the ODMR signals. It turns out that the + and – signs of the B_{mod}-ODMR signals are locked to the spin dependent PL, hence to the particular states involved in the transitions and to their populations: that is + for $m_s = 0 \leftrightarrow +1$, and – for $m_s = 0 \leftrightarrow -1$. This result was also found by comparing the symmetry of the ODMR signal corresponding to the $m_s = 0 \rightarrow +1$ and $m_s = 0 \rightarrow -1$ transitions for a fixed magnetic field direction (Fig. 2a). These finding together suggest that the B_{mod}-ODMR method is sensitive to the PL changes due to the out-of-equilibrium population of the m_s states; whereas the MW_{mod}-ODMR as well as the unmodulated ODMR methods are inherently insensitive.

3. Phenomenology of ODMR with magnetic field modulation

When a microwave radiation $B_1 \sin(\omega_0 t + \phi_0)$ with magnetic field B_1, frequency ω and phase ϕ_0 is scanned trough the region of resonances of a spin system, an absorption or emission of microwaves occurs generating a change in the amount of microwave power in the transmission line. In ODMR, the latter causes a change in the PL which is used for detection of electron spin transitions. When the spin system is placed in an external magnetic field (B_0) and an oscillating small magnetic field $B_m \sin(\omega_m t + \phi_m)$ is applied, the energy levels of the spin system are modulated and the PL signal oscillates at the same frequency. Lock-in phase sensitive detection is based on a mixer which multiplies the reference oscillating field and the PL signal, and after appropriate low-pass filtering enables the extraction of a first derivative-like signal with large suppression of background noise.

The effect of modulation field on the microwave signal is shown in Fig. 4a where ΔE indicates the difference between the microwave amplitude on and off resonance condition. For comparison, the effect of modulation microwave amplitude is also shown (Fig. 4b). The magnetic field modulation is transformed to PL modulation by conversion of the field $B_m \sin(\omega_m t + \phi_m)$ to a complex signal $F(\omega)$ which is a superposition of the fundamental modulation frequency ω_m and n harmonics [39]:

$$F(\omega) = \sum_{n=0}^{\infty} [a_n(\omega)\cos(n\omega_m t) + b_n(\omega)\sin(n\omega_m t)] \quad (1)$$

Each point of the PL signal can be described by these terms where at the inflection point is composed mainly by the fundamental term $b_n(\omega)\sin(n\omega_m t)$, at the maximum peak by the second harmonic $a_2(\omega)\cos(2\omega_m t)$ and for any other point by their combinations.

The only term responsible for the sign of the first derivative signal is the fundamental term $b_n(\omega)\sin(n\omega_m t)$ which is opposite for opposite sides of the absorption lineshape, whereas all the other terms and constants are always positive.

Thus, the first derivative signal is:

$$\Gamma(\omega < \omega_r) \propto +\sin(\omega_m t + \phi_m); \quad (2a)$$

$$\Gamma(\omega > \omega_r) \propto -\sin(\omega_m t + \phi_m); \quad (2b)$$

where Γ indicates the PL signal, ω_r is the resonance frequency and ϕ_m the modulation phase. Depending on ϕ_m the sign of the first derivative of the lock-in signal can be shifted from positive to negative and viceversa. For $\phi_m = \frac{\pi}{2}, \frac{3}{2}\pi$ then $S \equiv S_+, S_-$ respectively.

In the ODMR experiment with magnetic field modulation the $\phi_m = \frac{\pi}{2}, \frac{3}{2}\pi$ are locked to positive and negative magnetic fields respectively, thus resulting in: $\Gamma(\omega < \omega_r) > 0$ and $\Gamma(\omega > \omega_r) < 0$ for $\phi_m = \frac{\pi}{2}$; $\Gamma(\omega < \omega_r) < 0$ and $\Gamma(\omega > \omega_r) > 0$ for $\phi_m = \frac{3}{2}\pi$.

4. Proof-of-concept

The results reported above show that the ODMR spectral lines for each NV^- center change symmetry upon reversal of the magnetic field projection. These observations suggest that ODMR spectra recorded by demodulation of the magnetic field can be used for real-time detection of the magnetic field polarity.

Leveraging on this mechanism a method is provided for reading the polarity of a switching magnetic field simply monitoring the sign of a particular ODMR resonance line of one of the four inequivalent NV^- sites. A *proof-of-concept* experiment is shown in Fig. 5 where a square-wave voltage is applied to a coil placed in proximity of a diamond microcrystal. The current into the coil generates a $+\vec{B}$ or $-\vec{B}$ field at 1 Hz frequency, while an B_{mod}-ODMR signal is monitored as function of time at a fixed frequency ($\upsilon_r = 2866$ MHz) previously determined by measuring the ODMR spectrum at constant $|\vec{B}|$. The B_{mod}-ODMR signal at υ_r alternates with the same frequency of the square-wave B field, thus demonstrating real-time detection of magnetic field directions. For comparison, the MW_{mod}-ODMR spectrum remains constant albeit a small amplitude variation is observed due to the slight asymmetry of the magnetic field between parallel and anti-parallel directions.

Other methods have been developed for detection of magnetic field polarities with NV^- centers for scanning probe magnetometry. One method consists in applying a constant bias magnetic field which adds or subtracts to the sample's stray magnetic field. The magnetic field

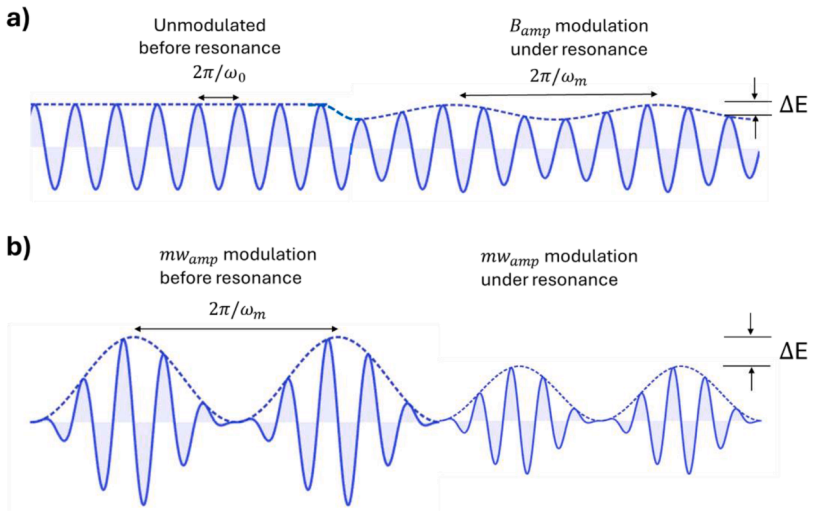

Fig. 4. Microwave signal before and during resonance absorption for magnetic field (**a**) and microwave amplitude (**b**) modulations. The absorption energy ΔE is indicated along with the magnetic field ($2\pi/\omega_0$) and microwave ($2\pi/\omega_m$) modulation frequencies.

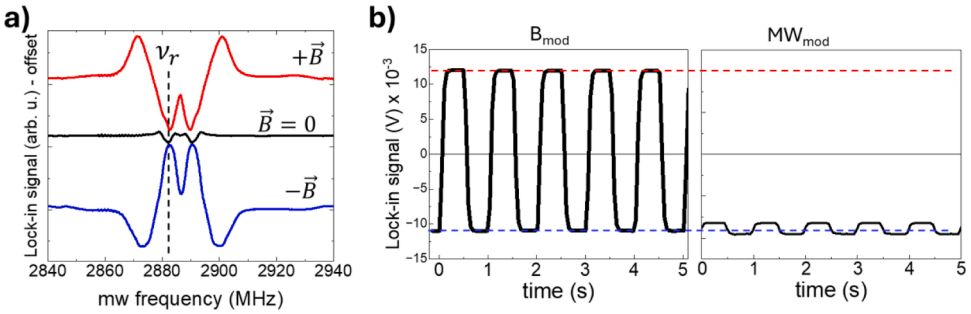

Fig. 5. a) *Proof-of-concept* for real-time detection of switching magnetic fields at 1 Hz frequency with B_{mod} and MW_{mod} (**b**) for a fixed resonance frequency ν_r indicated in **(a)**.

polarity can be determined by monitoring the changes of the ODMR signal at the maximum slope to higher or lower values caused by the shift of the resonance frequency. This method has been used by Maletinsky et al. with bias field of 5.2 mT to determine the sign of a magnetic field from bits of a magnetic memory [29], and by Rondin et al. to gain insights into the vortex structure of a ferromagnetic square-dot [40]. Another method relies on circularly polarized microwaves, σ^+ or σ^-: for a given polarization it is excited either the transition $m_s = 0 \rightarrow +1$ or $0 \rightarrow -1$, thus resulting in a resonance line in the ODMR spectrum at frequency $D + E/2$ or $D - E/2$ depending on the magnetic field polarity [28].

The method presented in this work offers key advantages compared to the ones mentioned above. Unlike the bias field method, the determination of the magnetic field with B_{mod}-ODMR is based on the sign of a resonance ODMR signal rather than the relative change of the PL signal. Thus, B_{mod}-ODMR is robust against small random fluctuations (*e.g.* jitter) of the resonance line and PL intensity which can lead to misreading of the magnetic field polarity. Furthermore, for enhanced sensitivity the bias field method requires a narrow resonance line which can be attainable in diamond with low density NV^- centers with a consequent $1/\sqrt{N}$ reduction of the ODMR contrast. Furthermore, B_{mod}-ODMR method requires linearly polarized microwaves which are fed to a simple transmission line (*e.g.* microwave striplines and patches). Instad, the method based on selected circularly polarized microwaves requires a more complex design of a resonator enabling fine tuning of the relative phase between two microwave feeding lines [28,41].

5. Conclusions

Magnetic field modulation ODMR spectra are observed for the first time in NV^- centers in the low magnetic field regime where the magnetic resonance spectral symmetries are found to be sensitive to the m_s states and population involved in the transitions as well as to the polarity of an external magnetic field. These finding deploy NV^- centers in diamond as sensor for direct static and dynamic detection of magnetic field polarities which can be implemented to spatial and temporal mapping of the magnetization distribution and dynamics in nanoscale magnetometry. Unlike other methods, B_{mod}-ODMR has no constraints for specific crystal orientation, it is robust against random fluctuations of the PL intensity, and does not requires an external bias magnetic field [42] or microwave resonators providing selective circular polarizations. Furthermore, this method can be implemented on advanced set-up with confocal microscopes as well as AFM scanning probes for imaging and magnetometry in material science, quantum technologies and beyond [43,44].

6. Materials and methods

Materials: 150 μm Red Fluorescent Microdiamond with concentration of $NV^- \sim 2.5$–3 ppm were purchased from Adámas NanoTechnologies Inc. A single crystal was glued on a microstripline.

Optical set-up: A diode pumped solid state (DPSS) laser (Thorlabs DJ532–40) mounted on a current and temperature controller (Thorlabs LDM56F and LDC200C) was used as optical excitation source. The laser beam was directed with a dichroic mirror to a 10x objective with nominal aperture 0.25. Photoluminescence was detected with a silicon

photodiode, 350 - 1100 nm, (Thorlabs, SM1PD1B), amplified with a transimpedance photocurrent amplifier (Thorlabs PDA200C) and sent to a MOKU:GO (Liquid Instruments) reconfigurable FPGA oscilloscope/ lock-in amplifier interfaced with a PC.

Microwave module: a microwave module was assembled with a ADF4351 generator (35 – 4400 MHz) controlled by microprocessor for adjustable frequency sweeps [45]. An SPDT rf switch was used for fast microwave power modulation. The microwave radiation was 40 dB broadband amplified (max output power 100 mW) for strong excitation and maximization of the ODMR contrast before feeding a microstripline made on a copper and FR4 dielectric board with thicknesses of 35 μm and 1.6 mm, respectively and terminated with 50 Ω load.

Magnets. NdFeB permanent magnets (Garnet s.r.l.) and coils with $N =$ 1000 turns and diameter 3 cm.

Data acquisition: Photoluminescence was detected on channel 1 of the oscilloscope as function of time while sweeping the microwave frequency whose start and stop frequency sweep logic input is fed into channel 2. The ODMR spectrum is built up by time to frequency conversion. Lock-in detection was made with time constant 20 ms (12 dB/ octave) and modulation frequency of 1 KHz (see **Figure S2**).

Data were analysed with *Origin professional* and *Matlab*.

Simulations: The spectra were simulated with EasySpin toolbox [46] from the diagonalization of the spin-Hamiltonian [47]:

$$\widehat{H} = g\mu_B \mathbf{B}\widehat{\mathbf{S}} + D\left(\widehat{S}_z^2 + S(S+1)\right) + E\left(\widehat{S}_x^2 + \widehat{S}_y^2\right) + \sum \widehat{\boldsymbol{S}}\boldsymbol{A}\widehat{\boldsymbol{I}}, \quad (3)$$

where g is the spectroscopic g-value, μ_B is the Bohr magneton, $\mathbf{B}$ is the magnetic field vector, $\widehat{\boldsymbol{S}}$ and $\widehat{\boldsymbol{I}}$ are the electron and nuclear spin operators, D and E are the zero-field splitting parameters and A_i is the hyperfine splitting between the triplet exciton and the i th nuclei. The first term is the Zeeman interaction, the second and third terms the zero-field splitting and the third term accounts for the hyperfine interactions. Fitting parameters for the spectrum in Fig. 2a where: $S = 1$, $g = 2$, $D =$ 2887 MHz, $E = 7$ MHz, $A = 2.5$ MHz, peak-to-peak linewidth $\Delta_{pp} = 2.3$ MHz, $B = 3.28$ mT, crystal symmetry = Fd-3 m, Euler angles = [150°, 110°, 28°], microwave propagation direction: $k \parallel z$. The result of the simulation proofs that the spectrum originates from negatively charged NV^- center in diamond with Fd-3m crystal symmetry resulting in four inequivalent sites due to the random substitution of a nitrogen atom next to a vacancy in a tetrahedral symmetry.

The spectra in Fig. 3a where simulated by using the Euler angles as fitting parameters. The external magnetic field was varied by less than 2.4 % around the average value of $B = 2.8$ mT to account for small misalignment of the microcrystal from perfect central position of the rotating permanent magnet. The external magnetic field was experimentally measured with an Hall probe 3.0 ± 0.5 mT and found to be consistent with the values used for the simulations.

CRediT authorship contribution statement

Fabrizio Moro: Writing – original draft, Methodology, Funding acquisition, Data curation.

Declaration of competing interest

The authors declare that they have no known competing financial interests or personal relationships that could have appeared to influence the work reported in this paper.

Acknowledgements

F.M. gratefully acknowledge financial support by Rete Interdipartimentale di Spettroscopia (project BIR2021) through the “fondi per le grandi attrezzature” University of Milano-Bicocca and PNRR MUR project (PE0000023-NQSTI).

Data availability

Data will be made available on request.

References

[1] M.W. Doherty, N.B. Manson, P. Delaney, F. Jelezko, J. Wrachtrup, L.C. L. Hollenberg, The nitrogen-vacancy colour centre in diamond, Phys. Rep. Rev. Sec. Phys. Lett. 528 (1) (2013) 1–45, https://doi.org/10.1016/j.physrep.2013.02.001.
[2] C. Kurtsiefer, S. Mayer, P. Zarda, H. Weinfurter, Stable solid-state source of single photons, Phys. Rev. Lett. 85 (2) (2000) 290–293, https://doi.org/10.1103/PhysRevLett.85.290.
[3] G. Balasubramanian, P. Neumann, D. Twitchen, M. Markham, R. Kolesov, N. Mizuochi, J. Isoya, J. Achard, J. Beck, J. Tissler, et al., Ultralong spin coherence time in isotopically engineered diamond, Nat. Mater. 8 (5) (2009) 383–387, https://doi.org/10.1038/nmat2420.
[4] H.J. Zheng, J.Y. Xu, G.Z. Iwata, T. Lenz, J. Michl, B. Yavkin, K. Nakamura, H. Sumiya, T. Ohshima, J. Isoya, et al., Zero-field magnetometry based on nitrogen-vacancy ensembles in diamond, Phys. Rev. Appl. 11 (6) (2019), https://doi.org/10.1103/PhysRevApplied.11.064068.
[5] J. Michl, J. Steiner, A. Denisenko, A. Bülau, A. Zimmermann, K. Nakamura, H. Sumiya, S. Onoda, P. Neumann, J. Isoya, et al., Robust and accurate electric field sensing with solid state spin ensembles, Nano Lett 19 (8) (2019) 4904–4910, https://doi.org/10.1021/acs.nanolett.9b00900.
[6] A. Laraoui, H. Aycock-Rizzo, Y. Gao, X. Lu, E. Riedo, C.A. Meriles, Imaging thermal conductivity with nanoscale resolution using a scanning spin probe, Nat. Commun. 6 (2015), https://doi.org/10.1038/ncomms9954.
[7] M.W. Doherty, V.V. Struzhkin, D.A. Simpson, L.P. McGuinness, Y.F. Meng, A. Stacey, T.J. Karle, R.J. Hemley, N.B. Manson, L.C.L. Hollenberg, et al., Electronic properties and metrology applications of the diamond NV^- center under pressure, Phys. Rev. Lett. 112 (4) (2014), https://doi.org/10.1103/PhysRevLett.112.047601.
[8] M.V.G. Dutt, L. Childress, L. Jiang, E. Togan, J. Maze, F. Jelezko, A.S. Zibrov, P. R. Hemmer, M.D. Lukin, Quantum register based on individual electronic and nuclear spin qubits in diamond, Science 316 (5829) (2007) 1312–1316, https://doi.org/10.1126/science.1139831.
[9] R. Schirhagl, K. Chang, M. Loretz, C.L. Degen, Nitrogen-vacancy centers in diamond: nanoscale sensors for physics and biology, Annu. Rev. Phys. Chem. 65 (2014) 83–105, https://doi.org/10.1146/annurev-physchem-040513-103659.
[10] A. Boretti, L. Rosa, J. Blackledge, S. Castelletto, Nitrogen-vacancy centers in diamond for nanoscale magnetic resonance imaging applications, Beilstein J. Nanotechnol. 10 (2019) 2128–2151, https://doi.org/10.3762/bjnano.10.207.
[11] A. Ajoy, P. Cappellaro, Stable three-axis nuclear-spin gyroscope in diamond, Phys. Rev. A 86 (6) (2012), https://doi.org/10.1103/PhysRevA.86.062104.
[12] D.V. Christensen, U. Staub, T.R. Devidas, B. Kalisky, K.C. Nowack, J.L. Webb, U. L. Andersen, A. Huck, D.A. Broadway, K. Wagner, et al., 2024 roadmap on magnetic microscopy techniques and their applications in materials science, J. Phys. Mat. 7 (3) (2024), https://doi.org/10.1088/2515-7639/ad31b5.
[13] M. Neupane, I. Belopolski, M.M. Hosen, D.S. Sanchez, R. Sankar, M. Szlawska, S. Y. Xu, K. Dimitri, N. Dhakal, P. Maldonado, et al., Observation of topological nodal fermion semimetal phase in ZrSiS, Phys. Rev. B 93 (20) (2016), https://doi.org/10.1103/PhysRevB.93.201104.
[14] F. Casola, T. van der Sar, A. Yacoby, Probing condensed matter physics with magnetometry based on nitrogen-vacancy centres in diamond, Nat. Rev. Mater. 3 (1) (2018), https://doi.org/10.1038/natrevmats.2017.88.
[15] G. Balasubramanian, I.Y. Chan, R. Kolesov, M. Al-Hmoud, J. Tisler, C. Shin, C. Kim, A. Wojcik, P.R. Hemmer, A. Krueger, et al., Nanoscale imaging magnetometry with diamond spins under ambient conditions, Nature 455 (7213) (2008) 648–U646, https://doi.org/10.1038/nature07278.
[16] L. Rondin, J.P. Tetienne, T. Hingant, J.F. Roch, P. Maletinsky, V. Jacques, Magnetometry with nitrogen-vacancy defects in diamond, Rep. Prog. Phys. 77 (5) (2014), https://doi.org/10.1088/0034-4885/77/5/056503.
[17] M. Chipaux, A. Tallaire, J. Achard, S. Pezzagna, J. Meijer, V. Jacques, J.F. Roch, T. Debuisschert, Magnetic imaging with an ensemble of nitrogen vacancy-centers in diamond, Eur. Phys. J. D 69 (7) (2015), https://doi.org/10.1140/epjd/e2015-60080-1.
[18] B.C. Cavenett, Optically detected magnetic resonance (ODMR) investigation of recombination processes in semiconductors, Adv. Phys. 30 (4) (1981) 475–538, https://doi.org/10.1080/00018738100101397.
[19] J.L. Luo, Y.F. Geng, F. Rana, G.D. Fuchs, Room temperature optically detected magnetic resonance of single spins in GaN, Nat. Mater. 23 (4) (2024), https://doi.org/10.1038/s41563-024-01803-5.
[20] P.G. Baranov, H.J. von Bardeleben, Semiconductors as studied by magnetic resonance methods, Appl. Magn. Reson. 39 (1–2) (2010) 1–2, https://doi.org/10.1007/s00723-010-0162-8.
[21] E. Sörman, N.T. Son, W.M. Chen, O. Kordina, C. Hallin, E. Janzén, Silicon vacancy related defect in 4H and 6H SiC, Phys. Rev. B 61 (4) (2000) 2613–2620, https://doi.org/10.1103/PhysRevB.61.2613.
[22] H. Kraus, V.A. Soltamov, F. Fuchs, D. Simin, A. Sperlich, P.G. Baranov, G. V. Astakhov, V. Dyakonov, Magnetic field and temperature sensing with atomic-scale spin defects in silicon carbide, Sci. Rep. 4 (2014), https://doi.org/10.1038/srep05303.
[23] H.L. Stern, Q.S. Gu, J. Jarman, S.E. Barker, N. Mendelson, D. Chugh, S. Schott, H. H. Tan, H. Sirringhaus, I. Aharonovich, et al., Room-temperature optically detected

magnetic resonance of single defects in hexagonal boron nitride, Nat. Commun. 13 (1) (2022), https://doi.org/10.1038/s41467-022-28169-z.
[24] V.Y. Ivanov, M. Godlewski, ODMR study of $Zn_{1-x}Mn_xSe/Zn_{1-y}Be_ySe$ and $(Cd_{1-x},Mn)Te/Cd_{1-y}Mg_yTe$ diluted magnetic semiconductor quantum wells, Appl. Magn. Reson. 39 (1–2) (2010) 31–47, https://doi.org/10.1007/s00723-010-0133-0.
[25] O. Gywat, H.A. Engel, D. Loss, R.J. Epstein, F.M. Mendoza, D.D. Awschalom, Optical detection of single-electron spin decoherence in a quantum dot, Phys. Rev. B 69 (20) (2004), https://doi.org/10.1103/PhysRevB.69.205303.
[26] E. Lifshitz, L. Fradkin, A. Glozman, L. Langof, Optically detected magnetic resonance studies of colloidal semiconductor nanocrystals, Annu. Rev. Phys. Chem. 55 (2004) 509–557, https://doi.org/10.1146/annurev.physchem.55.091602.094359.
[27] J.D. Breeze, E. Salvadori, J. Sathian, N.M. Alford, C.W.M Kay, Continuous-wave room-temperature diamond maser, Nature 555 (7697) (2018) 493, https://doi.org/10.1038/nature25970.
[28] T.P.M. Alegre, C. Santori, G. Medeiros-Ribeiro, R.G. Beausoleil, Polarization-selective excitation of nitrogen vacancy centers in diamond, Phys. Rev. B 76 (16) (2007), https://doi.org/10.1103/PhysRevB.76.165205.
[29] P. Maletinsky, S. Hong, M.S. Grinolds, B. Hausmann, M.D. Lukin, R.L. Walsworth, M. Loncar, A. Yacoby, A robust scanning diamond sensor for nanoscale imaging with single nitrogen-vacancy centres, Nat. Nanotechnol. 7 (5) (2012) 320–324, https://doi.org/10.1038/nnano.2012.50.
[30] R.A. Babunts, D.D. Kramushchenko, A.S. Gurin, A.P. Bundakova, M.V. Muzafarova, A.G. Badalyan, N.G. Romanov, P.G. Baranov, Features of high-frequency EPR/ESE/ODMR spectroscopy of NV-defects in diamond, Phys. Solid State 62 (11) (2020) 2024–2032, https://doi.org/10.1134/s1063783420110062.
[31] I.V. Zhukov, S.V. Anishchik, Y.N. Molin, ODMR spectroscopy of NV- centers in diamond under high MW power, Appl. Magn. Reson. 48 (11–12) (2017) 1461–1469, https://doi.org/10.1007/s00723-017-0933-6.
[32] L. Robledo, H. Bernien, T. van der Sar, R. Hanson, Spin dynamics in the optical cycle of single nitrogen-vacancy centres in diamond, New J. Phys. (2011) 13, https://doi.org/10.1088/1367-2630/13/2/025013.
[33] F. Moro, M. Moret, A. Ghirri, A.G. del Aguila, Y. Kubozono, L. Beverina, A. Cassinese, Room-temperature optically detected magnetic resonance of triplet excitons in a pentacene-doped picene single crystal, J. Mater. Res. 37 (6) (2022) 1269–1279, https://doi.org/10.1557/s43578-022-00536-y.
[34] P.A. Lane, L.S. Swanson, Q.X. Ni, J. Shinar, J.P. Engel, T.J. Barton, L. Jones, Dynamics of photoexticed states in C_{60}. An optically deteced magnetic resonance, ESR and light induced ESR study, Phys. Rev. Lett. 68 (6) (1992) 887–890, https://doi.org/10.1103/PhysRevLett.68.887.
[35] B.C. Rose, C.D. Weis, A.M. Tyryshkin, T. Schenkel, S.A. Lyon, Spin coherence and 14N ESEEM effects of nitrogen-vacancy centers in diamond with X-band pulsed ESR, Diamond Relat. Mater. 72 (2017) 32–40, https://doi.org/10.1016/j.diamond.2016.12.009.
[36] B.V. Yavkin, V.A. Soltamov, R.A. Babunts, A.N. Anisimov, P.G. Baranov, F. M. Shakhov, S.V. Kidalov, A.Y. Vul, G.V. Mamin, S.B. Orlinskii, Defects in nanodiamonds: application of High-Frequency cw and Pulse EPR, ODMR, Appl. Magn. Reson 45 (10) (2014) 1035–1049, https://doi.org/10.1007/s00723-014-0582-y.
[37] J. Harrison, M.J. Sellars, N.B. Manson, Optical spin polarisation of the N-V centre in diamond, J. Lumin. 107 (1) (2004) 245–248, https://doi.org/10.1016/j.jlumin.2003.12.020.
[38] R.J. Epstein, F.M. Mendoza, Y.K. Kato, D.D. Awschalom, Anisotropic interactions of a single spin and dark-spin spectroscopy in diamond, Nat. Phys. 1 (2) (2005) 94–98, https://doi.org/10.1038/nphys141.
[39] P.C. Poole, Electron Spin Resonance: A Comprensive Treatise on Experimental Techniques, New York J. Wiley, 1996.
[40] L. Rondin, J.P. Tetienne, S. Rohart, A. Thiaville, T. Hingant, P. Spinicelli, J.F. Roch, V. Jacques, Stray-field imaging of magnetic vortices with a single diamond spin, Nat. Commun. 4 (1) (2013) 2279, https://doi.org/10.1038/ncomms3279.
[41] J. Herrmann, M.A. Appleton, K. Sasaki, Y. Monnai, T. Teraji, K.M. Itoh, E. Abe, Polarization- and frequency-tunable microwave circuit for selective excitation of nitrogen-vacancy spins in diamond, Appl. Phys. Lett. 109 (18) (2016), https://doi.org/10.1063/1.4967378.
[42] D. Prananto, D. Kikuchi, K. Hayashi, Y. Kainuma, T. An, Imaging of stray magnetic field vectors from a magnetic particle with an ensemble of nitrogen-vacancy centers in diamond, Jpn. J. Appl. Phys. (2019) 58, https://doi.org/10.7567/1347-4065/ab2039.
[43] J.F. Barry, M.J. Turner, J.M. Schloss, D.R. Glenn, Y. Song, M.D. Lukin, H. Park, R. L. Walsworth, Optical magnetic detection of single-neuron action potentials using quantum defects in diamond, Proc. Natl. Acad. Sci. U.S.A. 113 (49) (2016) 14133–14138, https://doi.org/10.1073/pnas.1601513113.
[44] E. Boto, N. Holmes, J. Leggett, G. Roberts, V. Shah, S.S. Meyer, L.D. Muñoz, K. J. Mullinger, T.M. Tierney, S. Bestmann, et al., Moving magnetoencephalography towards real-world applications with a wearable system, Nature 555 (7698) (2018) 657, https://doi.org/10.1038/nature26147. -+.
[45] J. Stegemann, M. Peters, L. Horsthemke, N. Langels, P. Glösekötter, S. Heusler, M. Gregor, Modular low-cost 3D printed setup for experiments with NV centers in diamond, Eur. J. Phys. 44 (3) (2023), https://doi.org/10.1088/1361-6404/acbe7c.
[46] S. Stoll, A. Schweiger, EasySpin, a comprehensive software package for spectral simulation and analysis in EPR, J. Magn. Reson. 178 (1) (2006) 42–55.
[47] A. Abragam, B. Bleaney, Electron Paramagnetic Resonance of Transition Ions, Oxford University Press, 1970.